Charge-changing cross-section measurements of $^{12-16}$C at around 45A MeV and development of a Glauber model for incident energies 10A–2100A MeV

D. T. Tran,[1,2,*] H. J. Ong,[1,†] T. T. Nguyen,[3,4] I. Tanihata,[1,5] N. Aoi,[1] Y. Ayyad,[1] P. Y. Chan,[1] M. Fukuda,[6] T. Hashimoto,[7] T. H. Hoang,[1,2] E. Ideguchi,[1] A. Inoue,[1] T. Kawabata,[8] L. H. Khiem,[2] W. P. Lin,[9] K. Matsuta,[6] M. Mihara,[6] S. Momota,[10] D. Nagae,[11] N. D. Nguyen,[12] D. Nishimura,[13] A. Ozawa,[11] P. P. Ren,[9] H. Sakaguchi,[1] J. Tanaka,[1] M. Takechi,[14] S. Terashima,[5] R. Wada,[15,9] and T. Yamamoto[1]

(RCNP-E372 Collaboration)

[1]*Research Center for Nuclear Physics, Osaka University, Osaka, Japan*
[2]*Institute of Physics, Vietnam Academy of Science and Technology, Hanoi, Vietnam*
[3]*Pham Ngoc Thach University of Medicine, HCM, Vietnam*
[4]*Faculty of Physics and Engineering Physics, VNU-HCMUS, HCM, Vietnam*
[5]*School of Physics and Nuclear Energy Engineering and IRCNPC, Beihang University, Beijing, China*
[6]*Department of Physics, Osaka University, Osaka, Japan*
[7]*Institute for Basic Science, Daejeon, Korea*
[8]*Department of Physics, Kyoto University, Kyoto, Japan*
[9]*Institute of Modern Physics, Lanzhou, China*
[10]*Kochi University of Technology, Kochi, Japan*
[11]*Institute of Physics, University of Tsukuba, Tsukuba, Japan*
[12]*Dong Nai University, Dong Nai, Vietnam*
[13]*Tokyo University of Science, Tokyo, Japan*
[14]*Graduate School of Science and Technology, Niigata University, Niigata, Japan*
[15]*Cyclotron Institute, Texas A&M University, College Station, Texas, USA*

(Received 16 June 2016; revised manuscript received 4 November 2016; published 9 December 2016)

We have measured for the first time the charge-changing cross sections (σ_{CC}) of $^{12-16}$C on a ^{12}C target at energies below 100A MeV. To analyze these low-energy data, we have developed a finite-range Glauber model with a global parameter set within the optical-limit approximation which is applicable to reaction cross section (σ_R) and σ_{CC} measurements at incident energies from 10A to 2100A MeV. Adopting the proton-density distribution of ^{12}C known from the electron-scattering data, as well as the bare total nucleon-nucleon cross sections and the real-to-imaginary-part ratios of the forward proton-proton elastic scattering amplitude available in the literatures, we determine the energy-dependent slope parameter β_{pn} of the proton-neutron elastic differential cross section so as to reproduce the existing σ_R and interaction cross-section data for ^{12}C + ^{12}C over a wide range of incident energies. The Glauber model thus formulated is applied to calculate the σ_R's of ^{12}C on a ^{9}Be and ^{27}Al targets at various incident energies. Our calculations show excellent agreement with the experimental data. Applying our model to the σ_R and σ_{CC} for the so-called neutron-skin ^{16}C nucleus, we reconfirm the importance of measurements at incident energies below 100A MeV. The proton root-mean-square radii of $^{12-16}$C are extracted using the measured σ_{CC}'s and the existing σ_R data. The results for $^{12-14}$C are consistent with the values from the electron scatterings, demonstrating the feasibility, usefulness of the σ_{CC} measurement, and the present Glauber model.

DOI: 10.1103/PhysRevC.94.064604

I. INTRODUCTION

The nuclear sizes, usually defined by the root-mean-square (rms) charge or nucleon/matter distribution radii, are important nuclear quantities. The proton and neutron rms radii are not only important to extract information on the nuclear structure, but are also essential for extracting the neutron skin thickness, which offers an important means to constrain theoretical descriptions of the equation of state (EOS) of asymmetric nuclear matter [1]. The nuclear EOS is important to understanding the properties of dense nuclear matter such as the neutron stars as well as to predict supernovae and neutron star mergers [2].

Historically, the earliest evidence for a nuclear radius did not come from a direct measurement but was inferred from the studies of the α decay of radioactive nuclei [3]. It was only after 1950s, with the advent of particle accelerators and the quantum electrodynamics theory, that decisive evidences for finite nuclear sizes and more precise measurements of charge/proton radii became available. Scores of charge radii of mostly stable nuclei have since been precisely determined using electromagnetic probes such as the elastic scattering of fast electrons, x-ray spectroscopy of muonic atoms, and optical and K_α x-ray isotope-shift (IS) methods [4].

For short-lived unstable nuclei, the IS method had been the only source of information until very recently. The electron

*tdtrong@rcnp.osaka-u.ac.jp
†onghjin@rcnp.osaka-u.ac.jp

scattering which has been the most successful method to determine the nuclear charge radii is not applicable because the short-lived nuclei are not available as targets. While the effort to perform electron scattering on unstable nuclei is being pursued [5], it may take some time to achieve practical applications. The optical IS method, on the other hand, requires only a small number of atoms of the unstable nuclei. Experimentally, the IS measurements using laser spectroscopy have achieved very high precision (below 100 kHz) and sensitivity [6]. Spurred on by recent advances in computational methods, the IS methods have been successfully applied to determine the charge radii of light unstable nuclei up to ^{12}Be [7–12]. However, it is extremely challenging to apply the IS method to the $10 > Z > 4$ nuclei due mainly to insufficient precision in the atomic physics calculations and difficulty of production of low-energy isotopes.

In terms of other nonelectromagnetic probes, an important breakthrough was achieved in 1985 through the measurements of interaction cross sections of light neutron-rich nuclei, which led not only to the discovery of the neutron-halo structure [13] but also to the renaissance in nuclear physics with radioactive beams. By applying the Glauber model [14], the nuclear matter rms radii of neutron-rich He, Li, and Be isotopes were extracted for the first time [13]. Since then, interaction ($\sigma_{\rm I}$) as well as reaction cross sections ($\sigma_{\rm R}$) have been extensively measured, providing a wealth of information on the rms radii of the nuclear matter distribution of unstable nuclei up to the proton and neutron driplines [15]. Recently, by extending the Glauber-type analysis to the measured charge-changing cross section ($\sigma_{\rm CC}$), which is the total cross sections of all processes that change the proton number of a nucleus, Tanihata demonstrates [16], through comparisons with the results from the IS method, the feasibility of the $\sigma_{\rm CC}$ measurements to determine the point-proton distribution rms radii (referred to as "proton rms radii" hereinafter). Combining $\sigma_{\rm R}$ and $\sigma_{\rm CC}$ (or the proton rms radii determined by other electromagnetic probe), it is possible to determine the neutron distribution rms radii. The successful applications of the method to neutron-rich Be [17], B [18], and C [19] isotopes at incident-beam energy higher than 200A MeV mark an important milestone in the studies of nuclear radii.

The Glauber model has been the most widely used and successful method to determine matter rms radii of unstable nuclei. However, the applicability of this method at low-incident energies has been questionable. While the optical-limit approximation (OLA) of the Glauber model under the zero-range approximation (ZR) has proven to be the most economic and convenient model to calculate $\sigma_{\rm I}$ or $\sigma_{\rm R}$ at high incident energies [15], it failed to reproduce the experimental data at energies below 100A MeV. The discrepancy reaches almost 20% at a few tens of MeV per nucleon for the carbon isotopes [20]. Those discrepancies could be due to various possible effects such as the Fermi motion and Pauli correlations [21]. Taking into account the higher-order multiple scattering and Fermi-motion effects, Takechi *et al.* [22] modified the bare total nucleon-nucleon interaction cross sections and obtained calculations that reproduce the experimental $\sigma_{\rm R}$'s relatively well over a wide range of incident energies. Abu-Ibrahim and Suzuki [23], on the other hand, pointed out that the above-mentioned various effects would have been automatically included to some extent in formulating the profile function for the N-N scatterings.

In this paper, we report on the first measurement of the charge-changing cross sections ($\sigma_{\rm CC}$) of $^{12-16}$C on a ^{12}C target at incident energies at around 45A MeV. To analyze the data and extract the proton rms radii, we have developed a Glauber model within the optical-limit approximation (OLA), which is applicable to a wide energy range between 10A and 2100A MeV. Here, we determine the energy-dependent slope parameter β_{pn} of the proton-neutron elastic differential cross section, which is the only missing parameter besides the density distributions required in the Glauber model calculation. The β_{pp} parameter values for proton-proton scattering were adopted from the proton-proton scattering data. The extension of Glauber model to energies below 100A MeV is important because of the sensitivity of the low-energy $\sigma_{\rm R}$ (and perhaps $\sigma_{\rm CC}$) to the tail-density distributions of halo and skin nuclei. Such sensitivity has been demonstrated by the $\sigma_{\rm R}$'s of ^{11}Be on a ^{12}C and a ^{27}Al [24], as well as of ^{16}C on a ^{12}C target [25]. Applying the present Glauber model to calculate the reaction cross sections of the ^{12}C on a ^{9}Be and ^{27}Al targets, we demonstrate the reliability of our model. We also show that the extracted proton rms radii for $^{12-14}$C are consistent with the results from the electron scatterings.

II. EXPERIMENT

The experiment was performed at the exotic nuclei (EN) beam line [26], Research Center for Nuclear Physics (RCNP), Osaka University. Secondary $^{12-16}$C beams were produced in separate runs by fragmentation of a ^{22}Ne primary beam at 80A MeV incident on a ^{9}Be target with thickness ranging from 1.0 to 5.0 mm. The carbon isotope of interest was selected in flight by setting the appropriate magnetic rigidities of two dipole magnets of the EN fragment separator. A flat aluminum degrader, with thickness ranging from 0.3 to 5.0 mm, was placed at the first momentum-dispersive focal plane (F1) to improve the isotope separation of the secondary beams. The momentum acceptances of the secondary beams were typically set to $\pm 0.2\%$ using a set of collimators at F1. The secondary beams were angular focused at the second focal plane (F2), which is a momentum-achromatic and a charge-mass dispersive focal plane. The selected carbon-isotope beam was further purified using a set of collimators at F2 before being transported to and directed onto a 450-mg/cm^2-thick natural carbon target (reaction target) placed at the newly constructed third focal plane (F3) [27].

In the present work, we measured the $\sigma_{\rm CC}$'s of carbon isotopes employing the transmission method. Figure 1(a) shows the experimental setup at F3. The incoming carbon-isotope beam was identified on an event-by-event basis using the energy-loss (ΔE) and time-of-flight (TOF) method. ΔE was measured using a 320-μm-thick silicon detector, while the TOF between the ^{9}Be production target and the reaction target was determined using the timing information from a 100-μm-thick plastic scintillator placed right before the reaction target and the RF signal from the cyclotron. The timing signal from the plastic scintillator was also used as the trigger

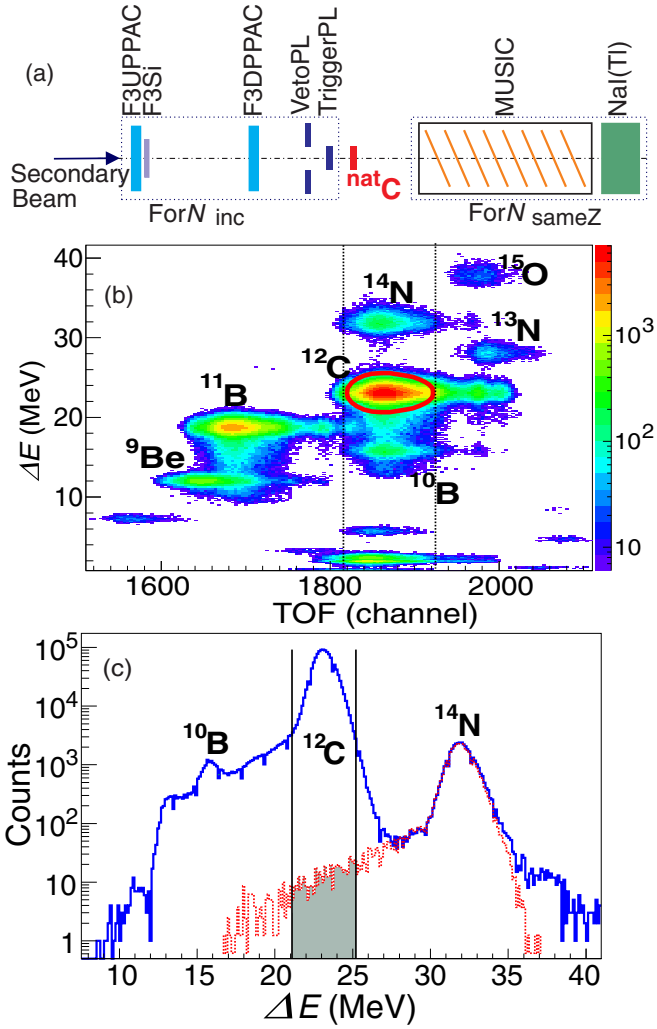

FIG. 1. (a) Schematic view of the experiment setup, (b) incoming ^{12}C beam identification, and (c) contaminant estimation.

for the data-acquisition system. Incident particles were tracked using the position information obtained with four parallel plate avalanche counters (PPACs) [28] located before F2 and F3. To select and define a good incident carbon-isotope beam, we rejected the particles that scattered at large angles after the last PPAC using a 3-mm-thick veto plastic scintillator, which has a square hole of a size smaller than the reaction target at its center, placed before the trigger scintillator. The remaining effects of materials other than the target, which include the plastic scintillator, were eliminated by empty target measurement. The number of good incident particles thus counted is denoted by $N_{\rm inc}$.

The outgoing particles went through the multisampling ionization chamber (MUSIC) [29], which consists of eight anodes and nine cathodes, before being stopped in a 7-cm-thick NaI(Tl) scintillator. The $\Delta E - E$ method was employed to identify and count the scattered particles. The Z-unchanged particles are counted and denoted by $N_{\rm sameZ}$.

III. DATA ANALYSIS AND RESULTS

In the transmission method, the $\sigma_{\rm CC}$ is calculated as follows: $\sigma_{\rm CC} = \ln[\gamma_0/\gamma]/t$, where t is the number of target nuclei per cm^2 of beam area and γ and γ_0 are the ratios of the number of the Z-unchanged particles and the number of incident particles, $\gamma = N_{\rm sameZ}/N_{\rm inc}$, of measurements with and without the reaction target respectively.

We determined the $N_{\rm inc}$ and $N_{\rm sameZ}$ using the information from the detectors before and after the reaction target respectively. Figure 1(b) shows a typical ΔE-TOF scatter plot for the secondary beams; the red ellipse shows the particle identification (PID) gate for ^{12}C. The contaminant in the PID gate was mainly the heavier isotopes with reduced energy losses due to the channelling effect in the silicon crystal. To estimate the amount of contaminant, we selected the TOF region as shown by the dotted lines in Fig. 1(b) and projected onto the ΔE axis. Figure 1(c) shows the projected ΔE distribution for the three nuclides with long tails due to the channeling effect. The contaminant (^{14}N) was identified and selected using the detector after the reaction target to obtain the shape of its ΔE distribution. By scaling the distribution to the one in Fig. 1(c) (red dotted spectrum), the contaminant (shaded area) was estimated to be less than 0.6% of $N_{\rm inc}$. Depending on the statistics of the carbon isotopes, the contaminants contribute to systematic uncertainties of only about 0.1–3.5 mb in the final cross sections and are much smaller than the errors of the cross sections.

The detection and particles identification of the Z-unchanged particles in the present reaction energies are more complicated than in the high energy due to energy loss straggling and multiple scatterings of the outgoing charged particles in the target and detector materials. The former results in broadening of the measured energy losses while the latter in reduced geometrical acceptance for the scattered-particle detectors. Figure 2 shows a typical $\Delta E - E$ plot for scattered particles obtained with the MUSIC (ΔE) and NaI(Tl) scintillator (E). The particles are classified by seven regions as shown in the figure: (1) beamlike particles, (2) elastic and inelastically scattered beamlike particles, (3) particles that reacted in the NaI(Tl) scintillator, (4) proton-picked-up particles, (5) proton-removed particles, (6) beam contaminants, and (7) out-of-acceptance particles, which were not detected by the NaI(Tl) detector. The number of particles with the same Z as the selected incident beam was determined by summing the events in the regions 1, 2, and 3. To estimate the number of light particles in region 3, a Gaussian peak plus an exponential background function was used to fit the experimental data (see the inset of the Fig. 2). The systematic uncertainties attributed to the background that contribute to the final $\sigma_{\rm CC}$'s are below 1 mb for all carbon isotopes.

The main source of systematic uncertainties lies in the estimation of the out-of-acceptance carbon isotopes in the region 7. The particles in the region 7 comprised about 2% of the total events, which include about 0.3% of the total Z-unchanged events. Simply adopting 0.3% as the systematic uncertainty results in as large as 20% uncertainty in the measured $\sigma_{\rm CC}$. Hence, to reduce this uncertainty, we have followed the suggestion in Ref. [30] and introduced an

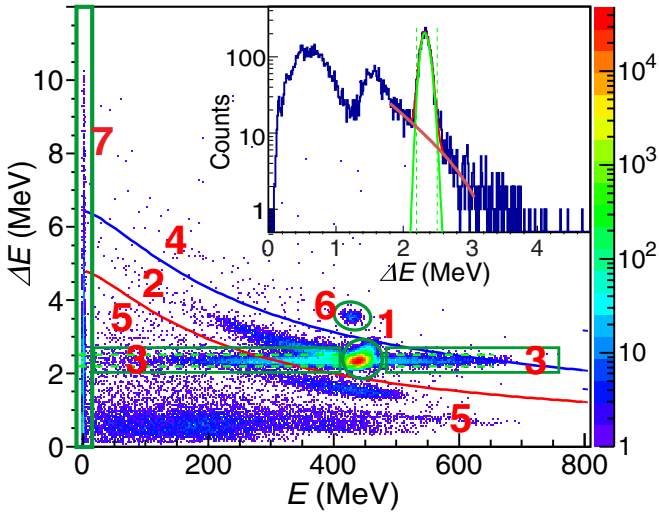

FIG. 2. Identification of the scattered particles. Inset: Estimation of the background contribution from region 5.

acceptance-correction factor, denoted by P. The final σ_{CC} was deduced as follows:

$$\sigma_{CC} = \frac{1}{t}\ln\left[\frac{\gamma_{out}(1-P_{in})}{\gamma_{in}(1-P_{out})}\right], \quad (1)$$

where the subscripts "in" and "out" indicate measurements with and without reaction target, respectively. Note the addition of the cross-section term, $\sigma_P = \ln[(1-P_{in})/(1-P_{out})]/t$, in Eq. (1). To demonstrate the importance of the acceptance correction, we plotted σ_P as functions of $1-P$ for several target thicknesses in Fig. 3(a). For simplicity, we have assumed $P_{out} = 0$. The solid line corresponds to our target thickness. The acceptance-correction factor depends on the beam energy, target thickness [30], as well as the configuration of the experimental setup. Therefore, it is important to consider this factor when designing an experiment.

P_i (i = in or out) was determined by assuming the scattering at large angle as being mainly due to the Rutherford scattering. To determine the experimental P_i, we first calculated the difference in the solid angles ($\Delta\Omega$) covered by a particular MUSIC electrode and the next layer (a MUSIC electrode or the NaI(Tl) scintillator) using the geometrical information of the experimental setup [see Fig. 3(b)]. By taking the event having an appropriate signal in one layer of the MUSIC but not in the next layer as the event being scattered into the solid angle $\Delta\Omega$, the number of lost events ΔN was determined for each scattering angle. The $\Delta N/(\Delta\Omega N_{inc})$ ratios thus obtained are proportional to the differential cross sections of the elastic Coulomb scattering, and were fitted with a calculated Rutherford scattering differential cross section distribution. As shown in the Fig. 3(c), the experimental data are well reproduced by the Rutherford distribution. To further confirm the assumption, we performed Monte Carlo simulations using the GEANT4 code [31]. The results from the simulations are also in excellent agreement with the experimental data as well as the Rutherford distribution. The P_i value is simply the integral of the distribution over the solid angles not covered by the NaI(Tl) detectors, as shown by the shaded area in Fig. 3(c). Depending on isotope, the P_{in} (P_{out}) value thus determined varies from 0.003 (0.0005) to 0.004 (0.0012), with an uncertainty between 2 and 10% (5 and 15%). These uncertainties contribute to 6–10 mb of σ_{CC} for different isotopes.

The determined σ_{CC} values are summarized in Table I. The uncertainties (in brackets) include the above-mentioned systematic uncertainties, the statistical uncertainties, as well as the uncertainty in the target thickness (0.06%). The results for ^{12}C at 38.0A-MeV incident energy, measured during the same experiment to examine possible systematic uncertainty due to the incident-beam energy, are also shown.

IV. FORMULATION OF THE GLAUBER MODEL

To extract the proton rms radii, we performed finite-range Glauber-model calculations within the OLA using the parameter set from nucleon-nucleon (N-N) cross sections. Following the procedures in Ref. [17] and ignoring the effect of neutrons in a projectile, we calculate σ_{CC} as follows:

$$\sigma_{CC} = 2\pi \int d\vec{b}[1 - |e^{i\chi(b)}|^2], \quad (2)$$

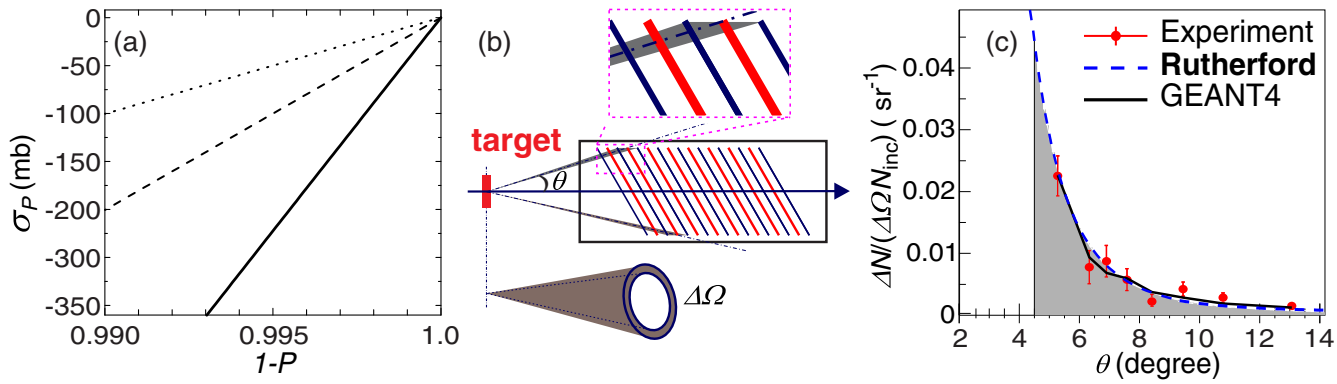

FIG. 3. (a) Effect of the acceptance-correction factor; the solid, dashed, and dotted lines correspond to 0.45, 1.0, and 2.0 g/cm^2 carbon target thicknesses, respectively. (b) Determination of θ and $\Delta\Omega$ from geometrical setup. The red- and blue-tilted lines are the anodes and cathodes respectively. (c) Acceptance-correction factor calculation. For details, see text.

TABLE I. The experimental values of σ_{CC} and proton rms radii of carbon isotopes.

	E (MeV/u)	σ_{CC} (mb)	r_p^{HO} (fm)[a]	r_p^{HO} (fm)[b]	r_p^{WS} (fm)[c]	$\bar{r}_p^{HO}$ (fm)	r_p^{ref} (fm)
^{12}C	38.0	1056(20)					
^{12}C	48.4	941(16)	2.35(6)	2.32(3)	2.33(8)	2.32(3)	2.327(7)[d]
^{13}C	47.7	968(39)	2.33(13)	2.33(4)	2.32(13)	2.33(3)	2.321(8)[d]
^{14}C	46.3	960(18)	2.27(6)	2.35(4)	2.36(9)	2.32(5)	2.370(11)[d]
^{15}C	44.1	987(34)	2.32(11)	2.41(4)	2.41(11)	2.39(8)	2.33(11)[e]
^{16}C	44.9	987(20)	2.32(7)	2.43(4)	2.45(10)	2.40(8)	2.25(11)[e]

[a]Determined from the σ_{CC}'s of this work.
[b]Determined from the σ_{CC}'s in the Ref. [32] using parameters in Table II.
[c]Determined using the σ_{CC}'s this work and Ref. [32] with WS-type density distribution.
[d]From Ref. [33].
[e]From Ref. [19].

where $\vec{b}$ is the impact parameter, and the exponential term is the transmission function given by the following relation:

$$e^{i\chi(b)} = \exp\left[\int_P\int_T \sum_N \left[\rho^z_{Pp}(\vec{s})\rho^z_{TN}(\vec{t})\Gamma_{pN}(\vec{b}+\vec{s}-\vec{t})\right]d\vec{s}d\vec{t}\right].$$

The superscript z in the above formula indicates the direction of integration, which corresponds to the direction of the incident particle, for the nucleon density. ρ^z_{Pp} is the proton density of the projectile and ρ^z_{TN} with subscript $N = p,n$ is the proton or neutron density of the target. $\vec{s}$ ($\vec{t}$) represents the two-dimensional coordinate of a particular projectile (target) nucleon relative to the center of mass of the projectile (target) nucleus, which lies on the plane perpendicular to the incident momentum of the projectile. Γ is the N-N amplitude [34], which in the case of the scatterings of protons off a nuclear target simplifies as the profile function [23]:

$$\Gamma_{pN}\left(\vec{b}\right) = \frac{1-i\alpha_{pN}}{4\pi\beta_{pN}}\sigma^{tot}_{pN}\exp\left[-\frac{b^2}{2\beta_{pN}}\right], \quad (3)$$

where α_{pN} is the ratio of the real to the imaginary part of the forward p-N scattering amplitude, β_{pN} is the slope parameter of the p-N elastic differential cross section, and $\sigma^{tot}_{pN}(E)$ is the total p-N cross section at incident energy E. The energy-dependent α_{pN} and β_{pN} parameters are interrelated, via the total elastic cross section $[\sigma^{el}_{pN}(E)]$ and $\sigma^{tot}_{pN}(E)$, as follows [35]:

$$\sigma^{el}_{pN}(E) = \frac{1+\alpha^2_{pN}}{16\pi\beta_{pN}}\left[\sigma^{tot}_{PN}(E)\right]^2. \quad (4)$$

In the OLA calculation, only the real part of the profile function that contains only the β_{pN} parameter contributes to the cross section. Hence, it is sufficient to determine β_{pp} and β_{pn} for the Glauber model calculations. Substituting the α_{pp} values and the cross sections from the Particle Data Group tabulation [36] into Eq. (4), we deduced β_{pp} over a wide range of incident energy. For β_{pn}, only a few data points for α_{pn} at incident energies above 174A MeV are available from Ref. [36]. Although parameter sets from the studies on proton-nucleus scatterings at proton energies ranging from 100 to 2200 MeV [34], and on heavy-ion scatterings at projectile energies 30A–350A MeV [37] are available, both parameter sets failed to reproduce the energy dependence of the reaction/interaction cross section of ^{12}C [22,38]. Introducing separate parametrization schemes for energies below and above 300A MeV, and adopting partially or modifying the parameters in Ref. [34], several authors have reported improved global systematics [22,38–40].

In this work, we took a different approach and determined the energy-dependent $\beta_{pn}(E)$, taking advantage of the accumulating experimental σ_R's [22] of ^{12}C on a ^{12}C target at incident energies from 10A MeV up to about 2100A MeV. To this end, we first fixed the proton- and neutron-density distributions which are needed for the OLA Glauber calculations. We adopted the sum-of-Gaussian distribution from the electron scattering data [41] as the proton density distribution in the ^{12}C target. For the neutrons, assuming a harmonic-oscillator (HO)–type density distribution, we determined the HO width parameter together with β_{pn} so as to reproduce the experimental σ_R [42] and σ_{CC} [43] of ^{12}C on a carbon target at around 950A MeV. We chose the data at this energy since the Glauber model is well established for high energies. Using these proton- and neutron-density distributions, we determined the $\beta_{pn}(E)$ so as to reproduce the experimental σ_R at various incident energies. The experimental σ_R data (black-open circles) and the "fitted" Glauber model calculation results (black solid line) are shown in Fig. 4(a). The best-fitted $\beta_{pn}(E)$ is shown in the inset. For reference, we listed the input parameters and the bare total nucleon-nucleon cross sections used in our Glauber model calculation in Table II.

V. RESULTS OF THE GLAUBER-MODEL ANALYSIS AND DISCUSSION

We applied the Glauber model to calculate the σ_{CC}'s at other energies. As shown in Fig. 4(a), the results show good agreement with the experimental σ_{CC}'s in the whole energy range including our measurements (red-filled squares). Using the same $\beta_{pn}(E)$ and density distribution of ^{12}C, we also calculated $\sigma_R(E)$ for ^{12}C on beryllium and aluminum targets. Again, we adopted the shape of distribution suggested from the electron-scattering data [41] for the proton density distributions of ^{9}Be and ^{27}Al. For the neutrons, we assumed a harmonic-oscillator (HO) plus Woods-Saxon (WS) shape for the Be and a WS shape density distributions for the Al target

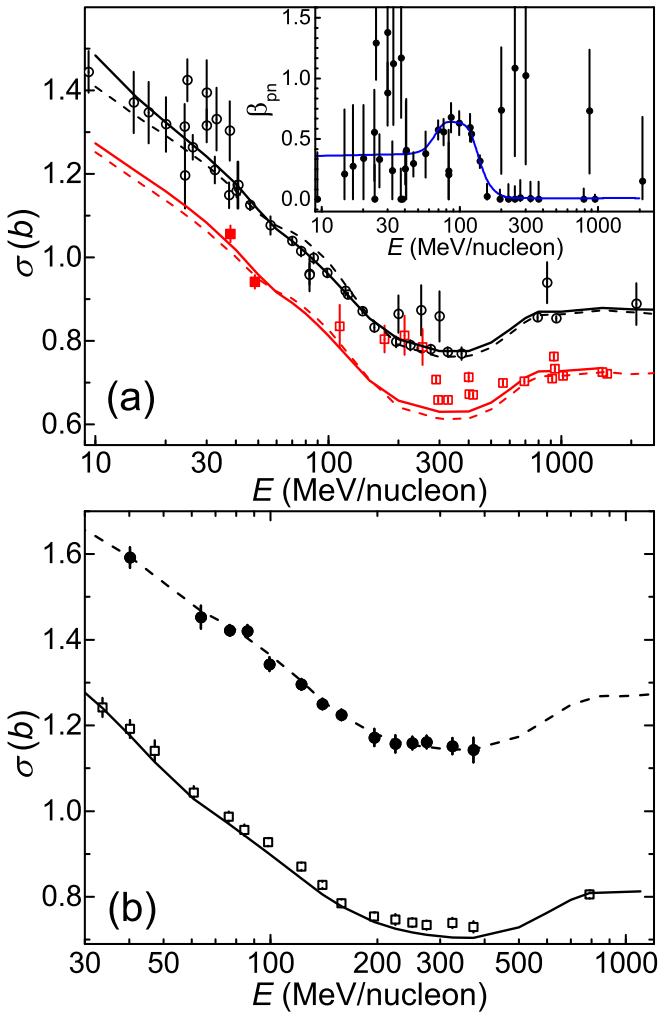

FIG. 4. (a) Experimental σ_R's (black open circles) [42,44–47] and σ_{CC}'s (red symbols) of ^{12}C on the carbon target. The red filled and red open squares are our data at 45A MeV and data from Refs. [17,43,48,49] respectively. The black solid line is the energy-dependent $\sigma_R(E)$ calculated with the best-fitted $\beta_{pn}(E)$ (inset) and HO-type neutron density distribution. The red solid line is the calculated $\sigma_{CC}(E)$. The dashed (black and red) lines are results of Glauber calculations [for $\sigma_R(E)$ and $\sigma_{CC}(E)$] with the OLA plus higher-order correction [50]. (b) Experimental σ_R's for ^{12}C on a beryllium (open squares) and aluminum (filled circles) targets. The solid and dashed lines are the $\sigma_R(E)$'s calculated with the present Glauber model. A neutron-density distribution with a tail structure is necessary for beryllium target. See text for the details on the input density distributions for the target nucleons.

nuclei, namely,

$$\rho_{Be} = \rho_{HO}(N=4, R_{Be}, r) + \rho_{WS}(N=1, R_{Be}, a_{Be}, r), \quad (5)$$

$$\rho_{Al} = \rho_{WS}(N=14, R_{Al}, a_{Al}, r), \quad (6)$$

where

$$\rho_{HO}(N,R,r) = \rho_0^{HO} \exp\left[-\left(\frac{r}{R}\right)^2\right]\left[1 + \frac{N-2}{3}\left(\frac{r}{R}\right)^2\right],$$

$$\rho_{WS}(N,R,a,r) = \frac{\rho_0^{WS}}{1+\exp\left[(r-R)/a\right]}.$$

TABLE II. Input parameters and bare total nucleon-nucleon cross sections for the Glauber model calculations.

E (MeV/u)	σ_{pp}^{tot} (mb)	β_{pp} (fm^2)	σ_{pn}^{tot} (mb)	β_{pn} (fm^2)
10	321.0	1.050	929	0.360
20	146.7	0.564	484	0.367
30	95.3	0.474	316	0.371
40	69.9	0.454	223	0.376
50	55.0	0.403	164.1	0.393
60	45.2	0.354	128.1	0.461
70	37.6	0.299	108.4	0.579
80	33.0	0.265	93.7	0.636
90	29.5	0.237	83.8	0.639
100	27.3	0.217	74.8	0.630
110	25.8	0.200	67.5	0.608
125	24.8	0.181	59.6	0.493
145	25.2	0.164	52.6	0.261
170	24.8	0.136	46.9	0.100
200	24.3	0.107	41.9	0.034
300	23.9	0.068	34.7	0.011
400	26.1	0.058	32.4	0.010
600	37.5	0.052	35.1	0.010
800	47.4	0.048	38.4	0.010
1000	47.5	0.049	38.2	0.010
1500	46.8	0.041	40.6	0.010
2200	45.0	0.037	40.8	0.010

ρ_0^{HO} and ρ_0^{WS} are normalization factors that conserve number of neutron(s). Here, we introduced the Woods-Saxon distribution with a tail density to account for the loosely bound valence neutron in ^{9}Be and determined the diffuseness as well as the HO width parameter for the ^{9}Be target so as to reproduce the experimental data at 33.6A [44] and 921A MeV [42]. For the ^{27}Al target, σ_R's at 40.2A and 372.4A MeV [44] were used to determine the WS parameters. As shown in Fig. 4(b), our calculations are in excellent agreement with the experimental data of ^{12}C on beryllium and aluminum targets. We note that calculations using the formulation [50] that includes higher order corrections to the OLA yield only slightly different results which are consistent with the OLA calculations within the experimental uncertainties [see the dashed lines in Fig. 4(a)].

Figure 5 shows the experimental σ_{CC}'s (red symbols) and σ_R's (black symbols) of ^{14}C [Fig. 5(a)] and ^{16}C [Fig. 5(b)] on a ^{12}C target. The red filled squares are our data at around 45A MeV. The red open squares are the data taken from Refs. [19,32,48]. The black open circles are the σ_R data taken from Refs. [25,42,46,47,51]. To calculate the $\sigma_R(E)$ and $\sigma_{CC}(E)$, and to extract the proton and neutron rms radii, we assumed HO-type proton-density distributions for the protons and neutrons in ^{14}C. We used the σ_R datum at 950A MeV [42], the σ_{CC} from Ref. [32], and our σ_{CC} to determine the HO width parameters for the proton- and neutron-density distributions. We have avoided using the σ_{CC} data other than the one from Ref. [32] shown in Fig. 5(a) because we found systematic deviations from our data for all $^{12-16}$C isotopes. We note that the σ_{CC} at around 930A MeV from Ref. [48] deviates as much as 7% from the datum at around 950A MeV from Ref. [43], which we have used together with the σ_R at 950A MeV to

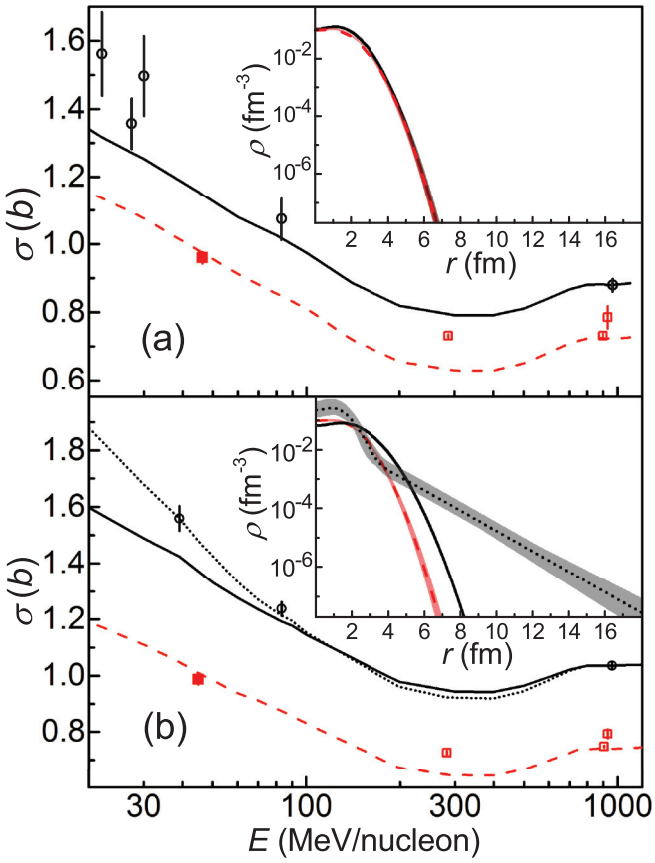

FIG. 5. Experimental σ_{CC}'s (red symbols) and σ_R's (black symbols) of (a) ^{14}C and (b) ^{16}C on a ^{12}C target. The red filled squares are our data at around 45A MeV. The red open squares are the data taken from Refs. [19,32,48]. The black open circles are the σ_R data taken from Refs. [25,42,46,47,51]. The red dashed and black lines correspond to the $\sigma_{CC}(E)$ and $\sigma_R(E)$ calculated using the present Glauber model. We assumed HO-type density distributions for the protons and neutrons in ^{14}C, as well as for the protons in ^{16}C. For ^{16}C, the neutron-density distribution with a HO core plus WS-type-two-neutron tail (core+2n) is necessary to reproduce the σ_R at energy below 100A MeV. The proton- and neutron-density distributions thus determined are shown in the insets: The red dashed (black solid) lines represent the HO-type proton- (neutron-) density distributions, and the black dotted line represents the core+2n neutron-density distribution. The hatched areas represent the uncertainties in the density distributions, which were determined from functional forms so as to reproduce the uncertainties of the measured cross sections.

determine the global parameters. As shown in Fig. 5(a), our calculations with the HO-type proton density distributions can reproduce our σ_{CC} and the datum at around 900A MeV [32]. The $\sigma_{CC}(E)$ and $\sigma_R(E)$ thus calculated are shown by the red dashed and black lines in Fig. 5(a).

For the ^{16}C isotope, a ^{14}C-core-plus-two-neutron–type nucleon density distribution has been suggested. Assuming such density distribution, Zheng *et al.* deduced a nucleon-density distribution with a relatively long tail [25]. Here, as a first trial, we assumed the HO-type density distributions similar to ^{14}C. The proton- and neutron-density distributions required to reproduce the experimental σ_R [42] and σ_{CC} [32] at around 950A MeV, as well as our σ_{CC}, are shown by the red dashed and black solid lines in the inset of Fig. 5(a) respectively. Obviously, the calculated $\sigma_R(E)$ underestimates the two experimental σ_R's at energies below 100A MeV. Such deviation is well known and has been observed in the reactions of ^{11}Be on ^{12}C and ^{27}Al at 33A-MeV incident energy [24]. To reproduce the experimental σ_R at low energy, we considered the HO core plus WS-type-two-neutron tail (core+2n) density distribution. The parameters for the core+2n neutron-density distribution were determined so as to reproduce the experimental σ_R's at 39A [47] and 950A [42] MeV. The core+2n density distribution thus deduced is shown by the black dotted line in the inset of Fig. 5(b). The calculation also reproduces the experimental data at 83A MeV [25] reasonably well. We note that similar neutron-density distribution, i.e., HO core plus WS-type-one-neutron tail (core+n), is also required to qualitatively explain the large σ_R data at energies below 100A MeV [47,51]. However, the large experimental uncertainties and the possible existence of systematic uncertainties in some of the data hinder any definitive conclusion. Hence, the present results confirm the importance of the σ_R (and perhaps the σ_{CC}) measurements at incident energies below 100A MeV.

The proton rms radii for $^{12-16}$C thus independently extracted from our measured σ_{CC}'s and the ones from Ref. [32] assuming the HO-type density distributions are shown in the fourth and fifth columns of Table I, respectively. The uncertainties shown in the brackets are from the uncertainties of the measured σ_{CC}'s as well as the systematic uncertainties of the functional forms chosen for the proton density distribution. Here, we have adopted the differences of about 0.5% between the central values of the proton rms radii determined with the HO- and WS-type functional forms as the systematic uncertainties; the diffuseness parameter, a, of the WS-type has been fixed to 0.55, which is recommended for light stable nuclei [41]. In the case the diffuseness is considered as a free parameter, the WS-type density distribution was determined so as to reproduce simultaneously the σ_{CC}'s of the present work and Ref. [51]. The proton rms radii thus determined are shown in the sixth column, together with the uncertainties which are attributed mainly to the larger uncertainty among the two measured σ_{CC}'s. The weighted averages of the proton rms radii determined from our σ_{CC}'s (the fourth column) and the ones from Ref. [32] (the fifth column) are shown in the seventh column ($\bar{r}_p^{HO}$). The uncertainties of the averaged proton rms radii include the uncertainties of σ_{CC}'s and their standard deviations. These uncertainties do not include the uncertainty of β_{pn}, which are mainly from σ_R's. In this energy region, the uncertainties of σ_R's are almost equivalent to that of our σ_{CC}. The inclusion of these uncertainties results in an additional uncertainty factor of about $\sqrt{2}$ in proton rms radii, which will not affect our conclusion. For comparison, the experimental proton rms radii for $^{12-14}$C from the electron-scattering data [33] and $^{15-16}$C from Ref. [19] are also shown. It is important to note that our results for $^{12-14}$C are in good agreement with, within one standard deviation from, the electron-scattering data including ones deduced from only low-energy measurement. These agreements provide further justification for the adoption of our experimental σ_{CC}'s in determining the proton rms radii.

The general consistencies between the experimental (σ_R and σ_{CC}) cross sections and our Glauber-model calculations with global parameters demonstrate the validity and versatility of the model for various isotopes over a wide range of incident energies.

VI. SUMMARY

In summary, we have measured the σ_{CC}'s of $^{12-16}$C on a carbon target using the transmission method at around 45A MeV incident-beam energies at the RCNP EN course, Osaka University. To analyze the low-energy data, we have developed a finite-range Glauber model with a global parameter set within the optical-limit approximation, which is applicable to incident energies below 100A MeV. Our calculations show excellent agreement with the experimental σ_R's for reactions of ^{12}C on a ^{9}Be and ^{27}Al targets. Performing the Glauber-model analysis on the experimental σ_R and σ_{CC}, we show the sensitivity of the low-energy σ_R to the tail-density distribution of neutron-haloor neutron-skin nuclei. The results confirm the importance of the σ_R (and perhaps σ_{CC}) measurements at incident energies below 100A MeV. We have also extracted the proton rms radii for $^{12-16}$C using our measured σ_{CC}'s, the recently published σ_{CC} data, and the existing σ_R data. The results for $^{12-14}$C are in good agreement with the values from the electron scatterings. These consistencies, together with the capability of our calculations to reproduce most of the experimental σ_R and σ_{CC} data for several isotopes and over a wide range of incident energies, demonstrate the usefulness of the σ_{CC} measurement and our Glauber model.

ACKNOWLEDGMENTS

We thank the RCNP Ring Cyclotron staff for delivering the ^{22}Ne beam stably throughout the experiment and Prof. K. Kimura for his precious advice during the preparation of the MUSIC detector. H.J.O. and I.T. would like to acknowledge the support of Prof. A. Tohsaki (Suzuki) and his spouse. D.T.T. and T.T.N. appreciate the support of RCNP Visiting Young Scientist Support Program. The support of the Vietnam Academy of Science and Technology under the Program of Development in the field of Physics by 2020-Study of unstable nuclei beam induced nuclear reactions in Japan, the PR China government and Beihang University under the Thousand Talent Program, and the support from the Nishimura and Hirose International Scholarship Foundations are gratefully acknowledged. This work was supported in part by JSPS-VAST Bilateral Joint Research Project and Grands-in-Aid for Scientific Research No. 20244030, No. 20740163, and No. 23224008 from Monbukagakusho, Japan.

[1] B. A. Brown, Phys. Rev. Lett. **85**, 5296 (2000).
[2] J. M. Lattimer, Annu. Rev. Nucl. Part. Sci. **62**, 485 (2012).
[3] G. Gamow and C. L. Critchfield, *Atomic Nucleus and Nuclear Energy Source* (Clarendon Press, Oxford, 1949).
[4] L. R. B. Elton, *Nuclear Sizes* (Oxford University Press, Oxford, UK, 1961).
[5] M. Wakasugi *et al.*, Nucl. Inst. Meth. Phys. Res. B **317**, 668 (2013).
[6] P. Campbell *et al.*, Prog. Part. Nucl. Phys. **86**, 127 (2016).
[7] L.-B. Wang, P. Mueller, K. Bailey, G. W. F. Drake, J. P. Greene, D. Henderson, R. J. Holt, R. V. F. Janssens, C. L. Jiang, Z.-T. Lu, T. P. O'Connor, R. C. Pardo, K. E. Rehm, J. P. Schiffer, and X. D. Tang, Phys. Rev. Lett. **93**, 142501 (2004).
[8] R. Sánchez, W. Nörtershäuser, G. Ewald, D. Albers, J. Behr, P. Bricault, B. A. Bushaw, A. Dax, J. Dilling, M. Dombsky, G. W. F. Drake, S. Gtte, R. Kirchner, H.-J. Kluge, Th. Kühl, J. Lassen, C. D. P. Levy, M. R. Pearson, E. J. Prime, V. Ryjkov, A. Wojtaszek, Z.-C. Yan, and C. Zimmermann, Phys. Rev. Lett. **96**, 033002 (2006).
[9] P. Mueller, I. A. Sulai, A. C. C. Villari, J. A. Alcántara-Núñez, R. Alves-Condé, K. Bailey, G. W. F. Drake, M. Dubois, C. Eléon, G. Gaubert, R. J. Holt, R. V. F. Janssens, N. Lecesne, Z.-T. Lu, T. P. ÓConnor, M.-G. Saint-Laurent, J.-C. Thomas, and L.-B. Wang, Phys. Rev. Lett. **99**, 252501 (2007).
[10] W. Nörtershäuser, D. Tiedemann, M. Žáková, Z. Andjelkovic, K. Blaum, M. L. Bissell, R. Cazan, G. W. F. Drake, Ch. Geppert, M. Kowalska, J. Krämer, A. Krieger, R. Neugart, R. Snchez, F. Schmidt-Kaler, Z.-C. Yan, D. T. Yordanov, and C. Zimmermann, Phys. Rev. Lett. **102**, 062503 (2009).
[11] A. Takamine, M. Wada, K. Okada, T. Sonoda, P. Schury, T. Nakamura, Y. Kanai, T. Kubo, I. Katayama, S. Ohtani, H. Wollnik, and H. A. Schuessler, Phys. Rev. Lett. **112**, 162502 (2014).
[12] A. Krieger, K. Blaum, M. L. Bissell, N. Frömmgen, Ch. Geppert, M. Hammen, K. Kreim, M. Kowalska, J. Krämer, T. Neff, R. Neugart, G. Neyens, W. Nörtershäuser, Ch. Novotny, R. Snchez, and D. T. Yordanov, Phys. Rev. Lett. **108**, 142501 (2012).
[13] I. Tanihata, H. Hamagaki, O. Hashimoto, Y. Shida, N. Yoshikawa, K. Sugimoto, O. Yamakawa, T. Kobayashi, and N. Takahashi, Phys. Rev. Lett. **55**, 2676 (1985).
[14] R. J. Glauber, in *Lectures in Theoretical Physics* (Interscience, New York, 1959), Vol. 1, p. 315.
[15] A. Ozawa *et al.*, Nucl. Phys. A **693**, 32 (2001).
[16] I. Tanihata *et al.*, Prog. Part. Nucl. Phys. **68**, 215 (2013).
[17] S. Terashima *et al.*, Prog. Theor. Exp. Phys. (2014) 101D02.
[18] A. Estrade *et al.*, Phys. Rev. Lett. **113**, 132501 (2014).
[19] T. Yamaguchi, I. Hachiuma, A. Kitagawa, K. Namihira, S. Sato, T. Suzuki, I. Tanihata, and M. Fukuda, Phys. Rev. Lett. **107**, 032502 (2011).
[20] M. Takechi *et al.*, Eur. Phys. J. A **25**, 217 (2005).
[21] N. J. DiGiacomo, R. M. DeVries, and J. C. Peng, Phys. Rev. Lett. **45**, 527 (1980); Phys. Lett. B **101**, 383 (1981).
[22] M. Takechi *et al.*, Phys. Rev. C **79**, 061601 (2009).
[23] B. Abu-Ibrahim and Y. Suzuki, Phys. Rev. C **62**, 034608 (2000).
[24] M. Fukuda *et al.*, Phys. Lett. B **268**, 339 (1991).
[25] T. Zheng *et al.*, Nucl. Phys. A **709**, 103 (2002).
[26] T. Shimoda *et al.*, Nucl. Inst. Meth. Phys. Res. B **70**, 320 (1992).
[27] I. Tanihata *et al.*, RCNP Ann. Rep. **17** (2011).
[28] H. Kumagai *et al.*, Nucl. Inst. Meth. Phys. Res. A **470**, 562 (2001).
[29] K. Kimura *et al.*, Nucl. Inst. Meth. Phys. Res. A **538**, 608 (2005).
[30] O. Yamakawa, Ph.D. thesis, Nagoya University, Nagoya, Japan, 1985 (unpublished).
[31] S. Agostinelli *et al.*, Nucl. Inst. Meth. Phys. Res. A **506**, 250 (2003).

[32] R. Kanungo *et al.*, Phys. Rev. Lett. **117**, 102501 (2016).
[33] I. Angeli and K. P. Marinova, At. Data Nucl. Data Tables **99**, 69 (2013).
[34] L. Ray, Phys. Rev. C **20**, 1857 (1979).
[35] Y. Ogawa *et al.*, Nucl. Phys. A **543**, 722 (1992).
[36] K. A. Olive *et al.* (Particle Data Group), Chin. Phys. C **38**, 090001 (2014) and 2015 update (see Fig. 50.9, p. 540).
[37] S. M. Lenzi, A. Vitturi, and F. Zardi, Phys. Rev. C **40**, 2114 (1989).
[38] W. Horiuchi, Y. Suzuki, B. Abu-Ibrahim, and A. Kohama, Phys. Rev. C **75**, 044607 (2007).
[39] B. Abu-Ibrahim *et al.*, Nucl. Phys. A **657**, 391 (1999).
[40] B. Abu-Ibrahim, W. Horiuchi, A. Kohama, and Y. Suzuki, Phys. Rev. C **77**, 034607 (2008).
[41] H. De Vries *et al.*, At. Data Nucl. Data Tables **36**, 495 (1987).
[42] A. Ozawa *et al.*, Nucl. Phys. A **691**, 599 (2001).
[43] W. R. Webber, J. C. Kish, and D. A. Schrier, Phys. Rev. C **41**, 520 (1990).
[44] M. Takechi, Ph.D. thesis, Osaka University, Osaka, Japan, 2006 (unpublished).
[45] C. Perrin, S. Kox, N. Longequeue, J. B. Viano, M. Buenerd, R. Cherkaoui, A. J. Cole, A. Gamp, J. Menet, R. Ost, R. Bertholet, C. Guet, and J. Pinston, Phys. Rev. Lett. **49**, 1905 (1982).
[46] H. Y. Zhang *et al.*, Nucl. Phys. A **707**, 303 (2002).
[47] D. Q. Fang *et al.*, Phys. Rev. C **61**, 064311 (2000).
[48] L. V. Chulkov *et al.*, Nucl. Phys. A **674**, 330 (2000).
[49] A. N. Golovchenko, J. Skvarč, N. Yasuda, M. Giacomelli, S. P. Tretyakova, R. Ilić, R. Bimbot, M. Toulemonde, and T. Murakami, Phys. Rev. C **66**, 014609 (2002).
[50] B. Abu-Ibrahim and Y. Suzuki, Phys. Rev. C **61**, 051601 (2000).
[51] D. Q. Fang *et al.*, Phys. Rev. C **69**, 034613 (2004).